

# Picosecond Imaging Of Bubbly Flows

Daniel A. Hunter<sup>1,\*</sup>, Philippe M. Bardet<sup>1</sup>

1: Dept. of Mechanical and Aerospace Engineering, The George Washington University, Washington D.C., United States

\*Corresponding author: [dahunter21@gwu.edu](mailto:dahunter21@gwu.edu)

**Keywords:** Multiphase Flows, Bubbly Flows, UltraFast Optics, Non-Linear Optics, Optical Kerr Effect.

## ABSTRACT

Despite their ubiquity, bubbly flows are notoriously challenging to instrument. In high-void fractions, most optical measurement techniques fail due to intense scattering and occlusion. Ultrafast imaging with picosecond exposure times offers an opportunity, allowing measurements before scattering obscures the field of view. Furthermore, detecting the time of arrival of photons allows measurement of bubble sizes, even for those partially occluded. Through implementing the Optical Kerr Effect (OKE), using a 70 fs 800 nm pulsed laser and a Carbon Disulfide cell, images are acquired with an exposure of 2.9 ps. Gating these images with an optical delay stage further allows the decomposition of scenes with 33 fs time increments. Proof of concept is demonstrated by applying this approach to static scenes of submerged bubbles at low and high void fractions. The experimental temporal decomposition shows the arrival of photons that travel through different media (air, water, and glass) and those scattered within the turbid media. A new visualization is presented to display this breakdown concisely, the Temporally Tagged Shadowgraph (TTS), presenting the time of arrival with the context of position and surroundings. Bubble sizes are measured using this temporal information and through edge detection, with good agreement for single unoccluded bubbles. With polydisperse bubble plumes, time delay-based measurements tend to overestimate bubble diameter; however, this could also be due to greater uncertainty in edge detection with occlusion. This demonstrates the potential of Ultrafast Imaging when it comes to probing high-void fraction flows. By further shortening exposure times and improving the robustness of processing algorithms, the scope of applicability of this technique can be widened.

---

## 1. Introduction

Air entrainment and gaseous exchange are essential processes for life. The oceans provide clear examples of such importance, acting as a critical artery for the climate, carbon capture and sequestration, and sea-spray aerosol generation. Much of the mass and energy transfer is due to breaking waves (Deike, 2022), generating plumes of submerged bubbles and clouds of aerosols. This is readily visible at the sea surface, with whitecap formation, owing to the dense scattering environment created, producing a diffuse white appearance. The overall wave-breaking process

is intrinsically complex, with underlying mechanisms in two deformable phases, length scales of  $\mathcal{O}(1 \text{ km} - 0.5 \mu\text{m})$ , and over a range of timescales.

Looking specifically at submerged bubbles, Deane & Stokes (2002) establish the bubble size distribution as the most critical property. This is well understood for low-void fractions and in the quiescent plume regime once bubble formation has ended. That said, experimental data for high void fraction plumes, including whitecaps and the initial formation phases, are lacking. Without this, crucial numerical models for wave breaking and its extended impact remain highly empirical. Considering the role of our oceans and the rapidly changing climate, improving the robustness of these models is imperative. High-void fraction air entrainment is not unique to wave breaking or the ocean. Similar entrainment is seen in a multitude of industrial and biological flows.

Conducting measurements with high void fractions is burdensome, especially at high speeds, explaining the lack of data. Invasive techniques can be helpful, albeit they disrupt the surrounding flow conditions, limiting deployment times and hindering long-term statistics. Optical, non-invasive, techniques are limited by the optically thick environment produced. Optical thickness measures the effective path length experienced by photons or the amount of attenuation occurring within a transmissive media. With high-void fractions with significant polydispersity, greater attenuation, and scattering, can be attributed to greater optical thickness.

Typical flow visualization techniques, including PIV, PLIF, and LTV, are suitable at low optical thicknesses owing to single-phase or low void fraction flows (Brückner, 2000). As void fraction and optical thickness increase, ghost PIV particles become more probable, and large occlusion regions make the above techniques unusable (Liu et al., 2020). Considerable efforts have increased robustness to occlusion within bubbly flows. Masuk et al. (2019) use tomographic virtual hull projections to simultaneously measure bubble size and track motion within a vertical bubble column. While effective, occlusion remains, leading to the overestimation of void fraction. Furthermore, tomographic approaches may not be suitable with limited optical access, or with distortion at the free surface. Belden et al. (2012) use a Synthetic Aperture, consisting of a 9-camera array, to diminish the effects of occlusion by sampling the light field from a dynamic bubble plume. This facilitated distribution measurements in time and space; however, they were only done at relatively low void fractions. Particle Shadow Velocimetry (PSV) has expanded the applicability of PIV within bubbly flows. By illuminating a volume and imaging in transmission, Bröder & Sommerfeld (2007) simultaneously tracked bubbles, estimating size and deformation, while concurrently extracting the surrounding flow field for void fractions up to 5%. Hessenkemper & Ziegenhein (2018) explored this further, raising the void fraction limit to 10%. Shadowgraphy employed, as with any view in transmission, tends to underestimate bubble size (Al-Lashi et al., 2016)(Chen et al., 2023). Due to scatterings at the bubble interface, edges become blurred, increasing uncertainty with edge detection and measurements.

Above an optical thickness of 10, X-ray radioscopic imaging has been used with great success, with

the smaller wavelengths allowing measurement within dense plumes of cramped bubbles and microbubbles (Aliseda & Heindel, 2021). There is, however, an untapped potential in the approximate optical thickness region between 2 and 10. Significant fragmentation and turbulent events produce these optical conditions; hence, conducting measurements in this region is essential. New measurement techniques are necessary, and Ultrafast Imaging presents prominent interest.

The refractive index describes the speed of photons as they pass through a media. Changes in refractive index at the interface between air and water causes incident light to scatter. By employing Lorenz-Mie Theory and the Deybe Expansion, Chaussonnet & Bardet (2020) numerically investigated the scattering of an ultrashort laser pulse caused by a small spherical bubble and compared the results to that of a droplet. By considering chromatic dispersion and pulse chirp caused by water, the influence of bubble depth and diameter over the optical response was established. Chaussonnet et al. (2021) took this further, using Monte-Carlo simulations to obtain the transient scattering response to a cloud of bubbles. This revealed a time delay between the detection of "Ballistic" photons passing through a bubble optical center, photons remaining undisturbed in water, and those undergoing multiple scatterings. Fig. 1 illustrates this phenomenon for bubbles of different sizes. At first order, the delay between ballistic and undisturbed photons presents at approximately 1.09 ps per millimeter of bubble diameter. Therefore, measuring this delay through ultra-high-speed imaging provides a mean to size bubbles. Doing so over a full plume can then produce distribution spectra. Capturing only the initial photons also removes the influence of intensity scattered photons, essentially probing a whitecap before it appears white.

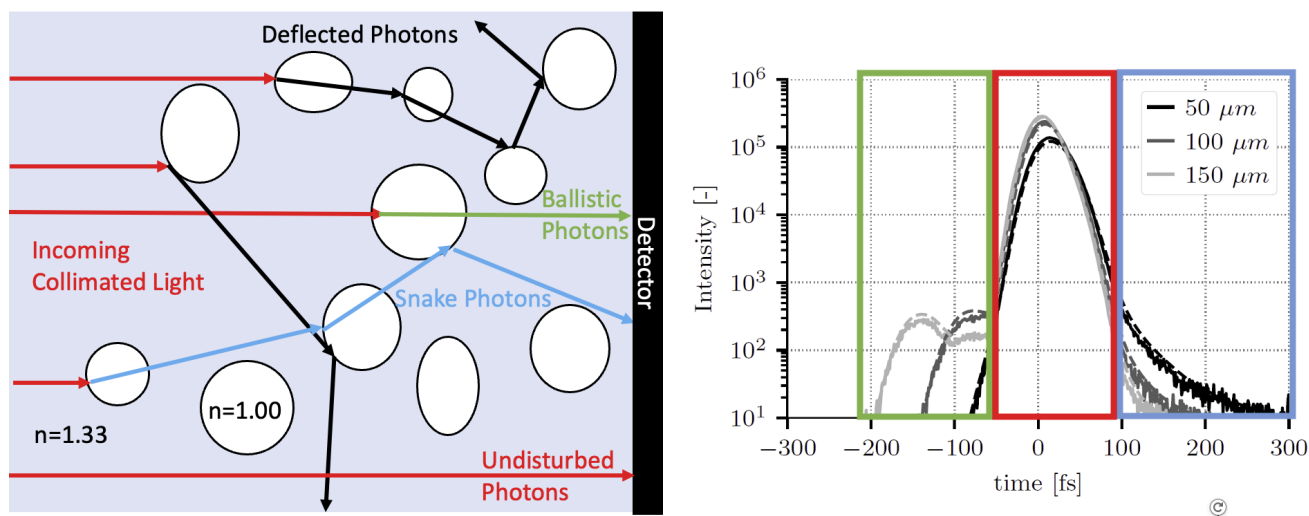


**Figure 1.** [Left] Diagram of rays passing through turbid bubbly media, highlighting the different paths experienced due to changes in geometry and refractive index [Right] Temporal response of intensity as a Gaussian ultrafast 800 nm pulse passes through a bubble of different size. Produced by Chaussonnet et al. (2021) through a computational Monte-Carlo model. Highlighted sections correspond to the paths demonstrated in [Left].

Similar ballistic imaging approaches have been used in the past with applications to particles and droplet sprays, (Linne et al., 2005; Calba et al., 2008; Sedarsky et al., 2006). To date, this has yet to

be applied to submerged bubbles. Showing initial proof of concept, this investigation has implemented the non-linear Optical Kerr Effect to probe low- and high-void fraction scenes. Building on the previous work of Chaussonnet & Bardet (2020) and Chaussonnet et al. (2021), a framework has been established for decomposing images temporally, revealing the time of arrival of light passing through different media. This also introduces the Temporally Tagged shadowgraph, an extension of traditional shadowgraphy, to represent the temporal location of photons and scattering modes within an image.

## 2. Experimental Set up

### 2.1. Optical Kerr Gating

In the presence of high-power laser beam, the refractive index of media exhibits a non-linear behavior. The first nonlinear term is expressed as (Boyd, 2008):

$$n = n_0 + \frac{3\chi^{(3)}}{4n_0} \langle \tilde{E}^2 \rangle \quad (1)$$

where  $n_0$  is the regular, "weak field," refractive index, and  $\chi^{(3)}$  is the third-order non-linear optical susceptibility,  $\langle \tilde{E}^2 \rangle$  is the time-averaged electric field strength squared. The Optical Kerr Effect (OKE) exploits this susceptibility and its influence over the total polarization state. High-energy light and its accompanying electric field activate the third-order non-linearity and change the refractive index, inducing birefringence. This non-linearity relaxes once the electric field is removed, restoring initial optical conditions. With birefringence, the incident light polarization ellipse will rotate, as demonstrated in Eq. (2).

$$\theta = \frac{1}{2} \Delta n \frac{\omega}{c} z \quad (2)$$

Where  $\Delta n$  refers to the induced birefringence,  $\omega$ , incident angular frequency,  $c$ , speed of light within media found with weak-field refractive index, and  $z$  path length through media. This rotation will cease once initial conditions are restored. The settling, or switching, time of a Kerr media is a function of the activation mechanism of the third-order non-linearity. For example, Carbon Disulfide ( $\text{CS}_2$ ), a standard Kerr media where  $\chi^{(3)} = 3.1 \times 10^{-20} \text{ m}^2/\text{V}^2$  at 532 nm (Chase & Van Stryland, 1995), induces nonlinear changes through molecular reorientation. Due to the molecular prolate spheroid shape, this reorientation exhibits a characteristic switching time,  $\tau_o$ , between 1-2 ps (Shapiro & Broida, 1967; Mourou & Malley, 1975; Eisenthal, 1977; Idlahcen et al., 2009). The orientational switching response is a temporal function of  $\tau_o$ , incident pulse width,  $T_w$ , and input peak electric field strength,  $E_0$ . This is simplified in Eq. (3) (Sala & Richardson, 1975).

$$\frac{\Delta n^o(t)}{E_0^2} = c n_0^o \frac{\pi^{1/2} T_w}{2K \tau_o} \exp\left(-\frac{t}{\tau_o} + \left(\frac{T_w}{2K\tau_o}\right)^2\right) \times \text{erfc}\left(-\frac{Kt}{T_w} + \frac{T_w}{2K\tau_o}\right) \quad (3)$$

Here  $K = [4 \ln 2]^{1/2}$  and  ${}_e n_2^o$  is the first-order corrected orientational Kerr coefficient, which is related to  $\chi^{(3)}$ . Pairing this  $\text{CS}_2$  switching phenomenon with two perpendicular polarizers creates an Optical Kerr Gate, which is essentially a non-linear external shutter (Fig. 2). Here, the shutter exposure time is a function of the material response to excitation. Given the ultrashort characteristic switch time, exciting the  $\text{CS}_2$  with an ultrafast laser pulse will produce picosecond exposure times, allowing the aforementioned time of arrival measurement.

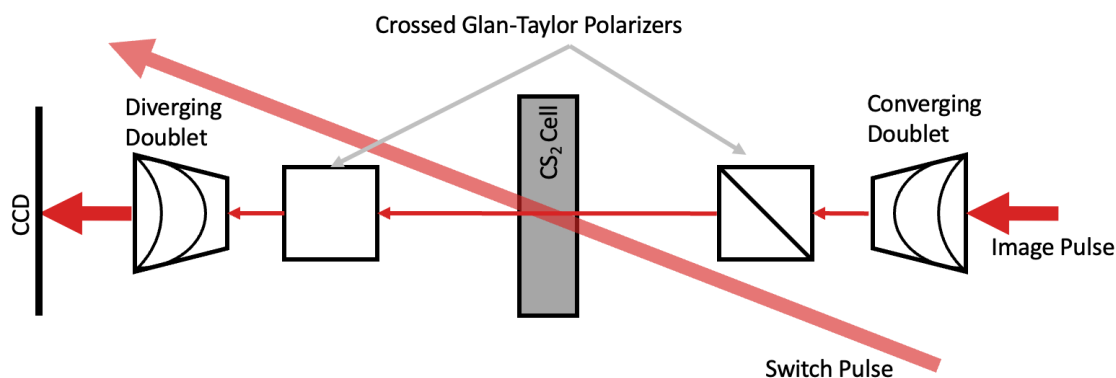


**Figure 2.** Simplified layout of an Optical Kerr Gate, showing the switching pulse, which opens the shutter through creating birefringence, and the image pulse, transmitting an image to CCD.

## 2.2. Optical Arrangement and Test Cases

In line with the simulations of Chaussonnet & Bardet (2020) and Chaussonnet et al. (2021), both imaging and Kerr Cell switching utilize an Amplified Ti:Sapphire pulsed laser (Coherent<sup>®</sup> Astrella), producing 70 fs 800 nm pulses at 1 kHz and up to 7 mJ. The optical arrangement employed is similar to that of Linne et al. (2005). Following emission, the beam is split 80:20, with the more intense pulse used for switching. The weaker probe pulse passes through an optical delay stage (ThorLabs<sup>®</sup> ODL100), allowing control of the probe pulse arrival time with a temporal resolution of 33 fs. After a delay, the probe pulse passes through a quarter wave plate and a lens tube telescope system to illuminate a small test section. In the test section, a static or dynamic bubbly flow will scatter the probe pulse as described by Chaussonnet et al. (2021). This deformed pulse is then focused through a second telescope system before entering the optical Kerr gate (OKG).

Concurrently, two ultrafast enhanced silver coated mirrors reflect the intense switch pulse towards the Kerr gate. Both pulses arrive at the Kerr gate in close succession, with the optical path lengths of each pulse being equal. The Kerr cell, as described previously, is comprised of two Glan-Taylor Polarizers (ThorLabs<sup>®</sup> GT10-B) centered around a  $50 \times 35 \times 10$  mm macro cuvette, filled with anhydrous  $\text{CS}_2$ . Birefringence is induced upon the switching pulse arriving at the cuvette at an angle,

$\theta$ , of approximately  $14^\circ$  to the normal and probe pulse. Once birefringent, the polarization state of the deformed image pulse is rotated, allowing transmission through the second polarizer. After passing through a neutral density filter (OD 1), the transmitted image is focused through a 200 mm camera lens (Nikon AF Micro-NIKKOR 200 mm f/4D IF-ED). Focused images are captured using a Teledyne Dalsa Genie™ Nano-M1930-NIR camera.

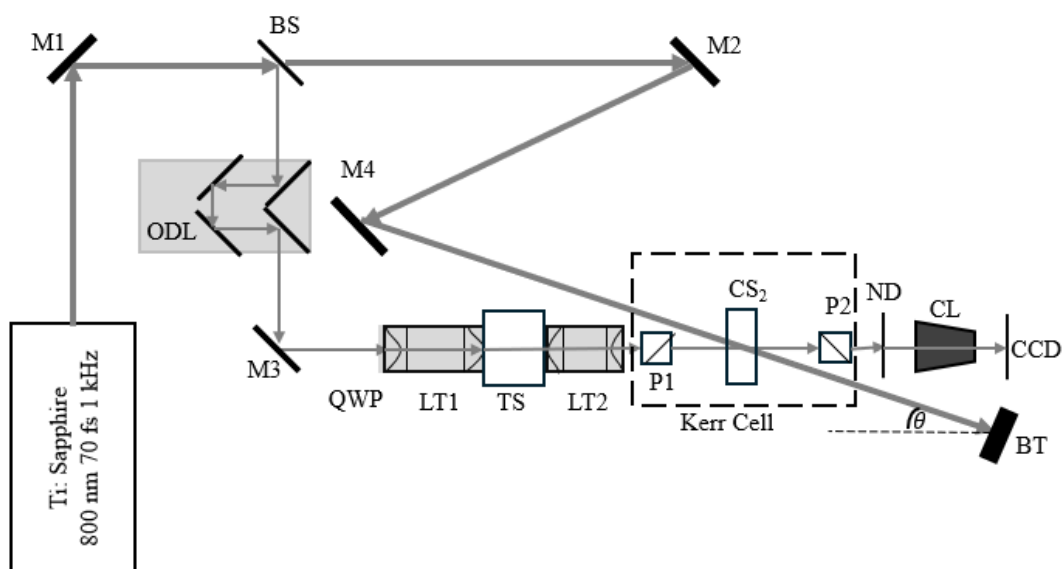
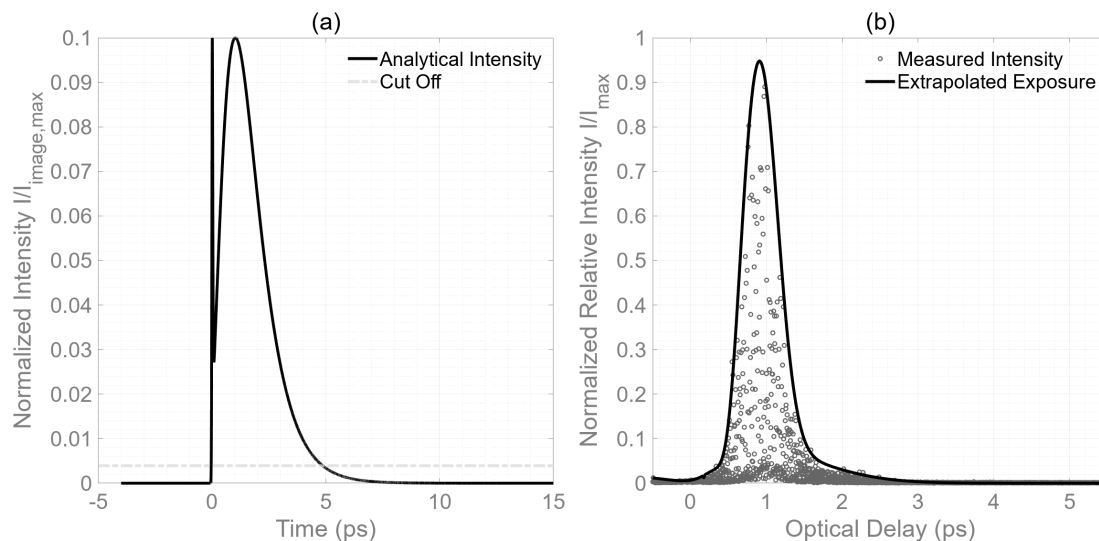


Figure 3. Optical layout diagram

The combination of the 1.86 ps switch time for  $\text{CS}_2$ , as measured by Shapiro & Broida (1967), 70 fs Gaussian switch pulse with a 2.0 mJ/pulse power and ND filter control the observed exposure. At first order, using Eqs. (2,3) and assuming the birefringence across the 10 mm cuvette is uniform at the same instant, produces an exposure of 4.9 ps (Fig. 4(a)). When determined experimentally, the actual exposure is closer to 2.9 ps. While this is more than double the 1.09 ps delay per mm, using the 33 fs time steps of the delay stage, time-gated images at this finer resolution.

Static two-phase scenes were imaged and temporally decomposed to show initial experimental proof of concept. Initially, a thick-walled glass rod (1.2 mm ID, 6 mm OD) was used to create a stable submerged air bubble. This produces stable, nonspherical bubbles of unknown size, which can be determined with traditional shadowgraphy and the time-resolved approach. A more complex yet realistic scene was also created, with the aid of a refractive index-matched polymer (MY Polymers® MY-133-V2000) (Fig. 9). A static high-void fraction, poly-disperse bubble plume, is produced by injecting air into the uncured polymer, agitating, and quickly curing with a UV laser. Once cured, the polymer exhibits a refractive index of 1.331 at 800 nm, slightly higher than pure water (Chaussonnet et al., 2021). At first order, this change in refractive index will not change the measured time delays significantly, producing a delay of 6.6 fs/mm delay between the polymer and water. This difference is undetectable for bubbles less than 5 mm in diameter with the current



**Figure 4.** (a) First order Analytical solution of intensity produced by Optical Kerr Gate of 10 mm CS<sub>2</sub> triggered by a 70 fs 2 mJ pulse. (b) Experimentally measured intensity profile, showing a decrease in exposure time from that calculated analytically.

hardware.

### 3. Results and Discussion

#### 3.1. Single Stable Bubble

The complete temporal history of the static bubble scene is achieved by acquiring images at 1 kHz while the delay stage is moved at a constant speed of 5.9981 ps/s. This produces an observed frame rate of 166.7 frames/ps (166.7 THz). With the bubble being stationary and stable, this was repeated with the camera aperture incrementally closed to extend the dynamic range. One thing of note is the multiple responses as the delay optical delay changes. Due to reflections within the test section and from the CS<sub>2</sub> cell, additional weaker responses are seen as relative time delay increases (Fig. 5). To avoid the influence of these back reflections, only the first appearing response is used for analysis; select frames from this response are shown in Fig. 6.

In agreement with Chaussonnet & Bardet (2020), the optical center of the bubble first becomes visible (Fig. 6a). The almost spherical bubble geometry, accompanied by the change in the refractive index, creates a lensing effect, and incident rays become focused at the center. This focusing is observable with the change of shape and intensity of the ballistic signal while visible. Following the ballistic signal, the surrounding undisturbed photons begin to appear. Fig. 6(b) and (c) show both the ballistic signal and undisturbed signals appearing simultaneously, a consequence of the 3 ps exposure, and the almost three orders of magnitude difference in peak intensity (Fig. 1). The distinction between the location of these two signals becomes more apparent with a smaller aperture

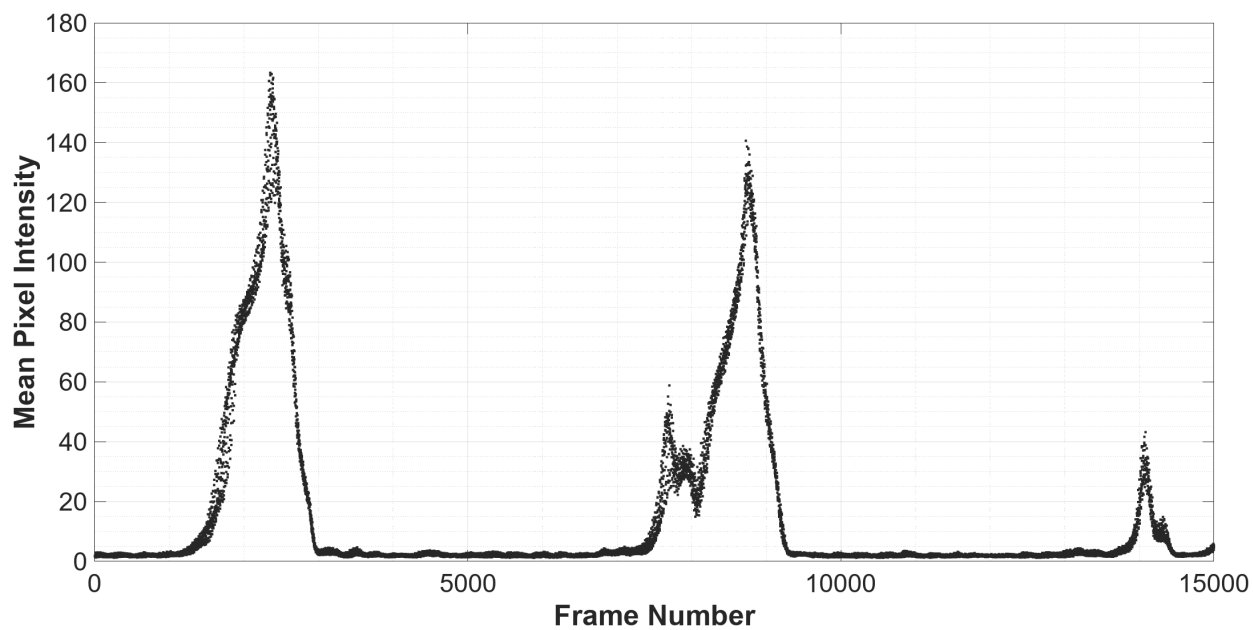


Figure 5. Mean pixel intensity for 15000 frames, showing multiple responses.

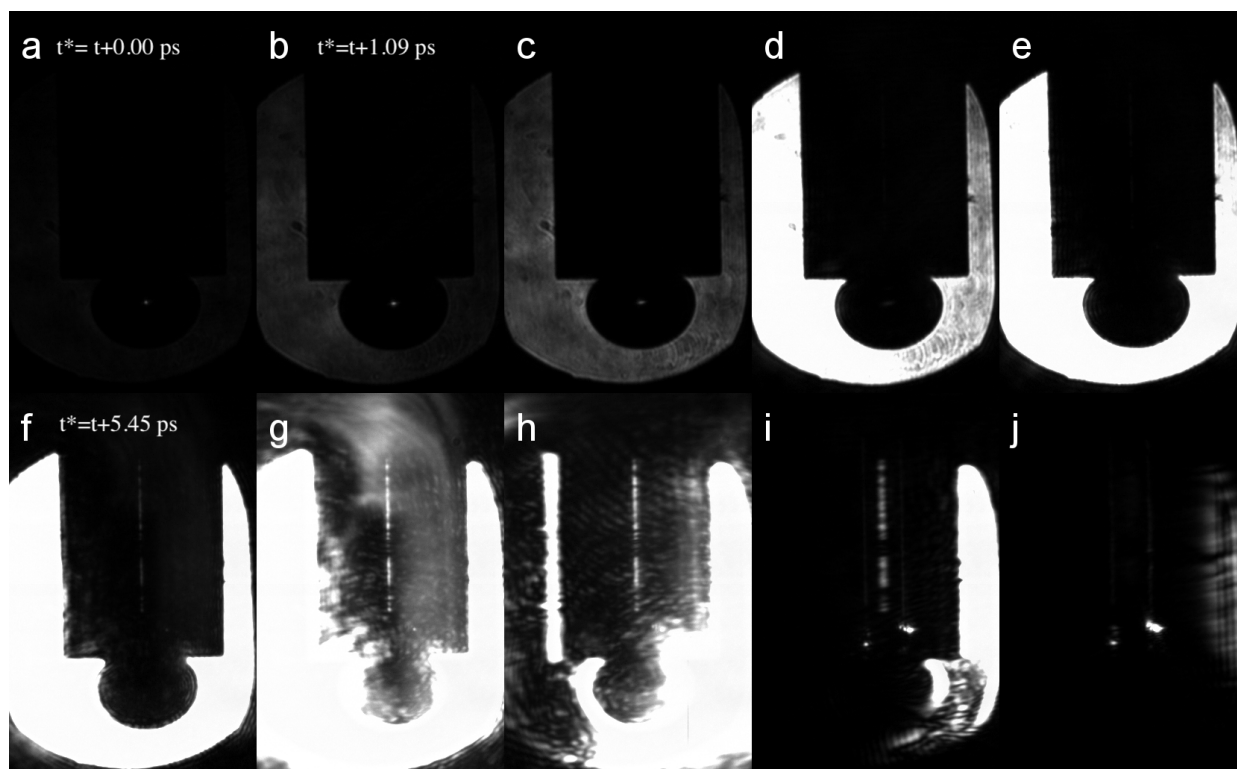
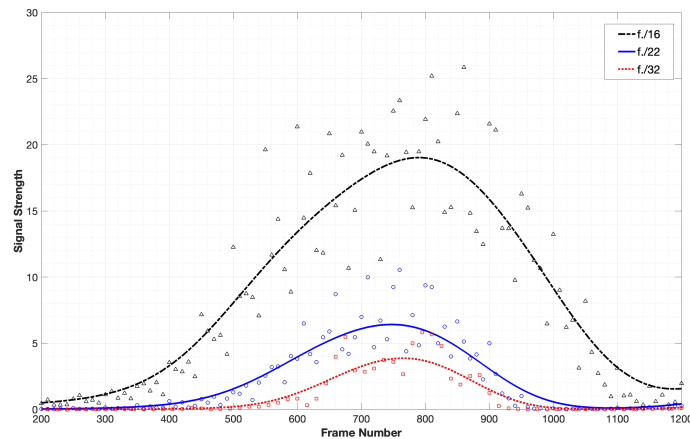


Figure 6. Montage of OKE time-gated images of a single bubble stabilized on a thick glass rod. Displayed frames are spaced in 1.09 ps intervals.

(Fig. 7). Ballistic signal intensity is diminished, only becoming noticeable at its peak, aiding size determination. That said, lower image pulse power and smaller bubbles result in ballistic signals becoming undetectable.



**Figure 7.** Comparison of the mean ballistic signal for constant power for three different apertures.

While the ballistic signal fades, the undisturbed signal increases intensity, reaching a peak and leaving only shadows of the bubble and rod. Following this peak, shadows lose definition as higher-order scattering modes become prominent (Fig. 6f). Fringe patterns appear in conjunction with this scattering (Fig. 6g), losing significant definition. The center of the glass rod becomes visible at this time. Like the bubble, the rod acts as a cylindrical lens, focusing incident light at its center. Glass has a higher refractive index than water, hence this signal is expected to arrive after the undisturbed signal. The surrounding fringes partially occlude its initial appearance, however it becomes clearer in Fig. 6(h). Further progression shows the surrounding water signal rapidly fading, which is not uniform. Instead, a horizontal scanning effect is noticeable. Idlahcen et al. (2009) attribute these spatiotemporal variations to the angle of incidence of the switching pulse. There is, therefore, an internal time delay within the image, with the left of the image appearing first.

Notably, in Fig. 6(h) and (i), the outlines of both the bubble and rod linger slightly after the signal fades. This again coincides with Chaussonnet & Bardet (2020), where scattering modes are still after the disappearance of the ballistic signal. As the image continues to fade, only scattering and defocusing from defects in the glass rod remain visible before the signal ultimately diminishes.

Through acquiring this series of frames, each pixel can be treated as an independent time series. Delays between peak intensity, used to determine size, may be found with time-series analysis techniques, notably cross-correlation. First, the center of the bubble is located and assumed to be the location of the ballistic signal. Taking this as a common reference, assigning  $t = 0$ , the time delay for all remaining signals is computed relative to the ballistic signal. This differs from Chau-

sonnet & Bardet (2020), where  $t = 0$  is assigned to the peak undisturbed signal. Compiling the time delays of all pixels and masking to only objects of interest reforms the image in a Temporally Tagged Shadowgraph (TTS) (Fig. 8b).

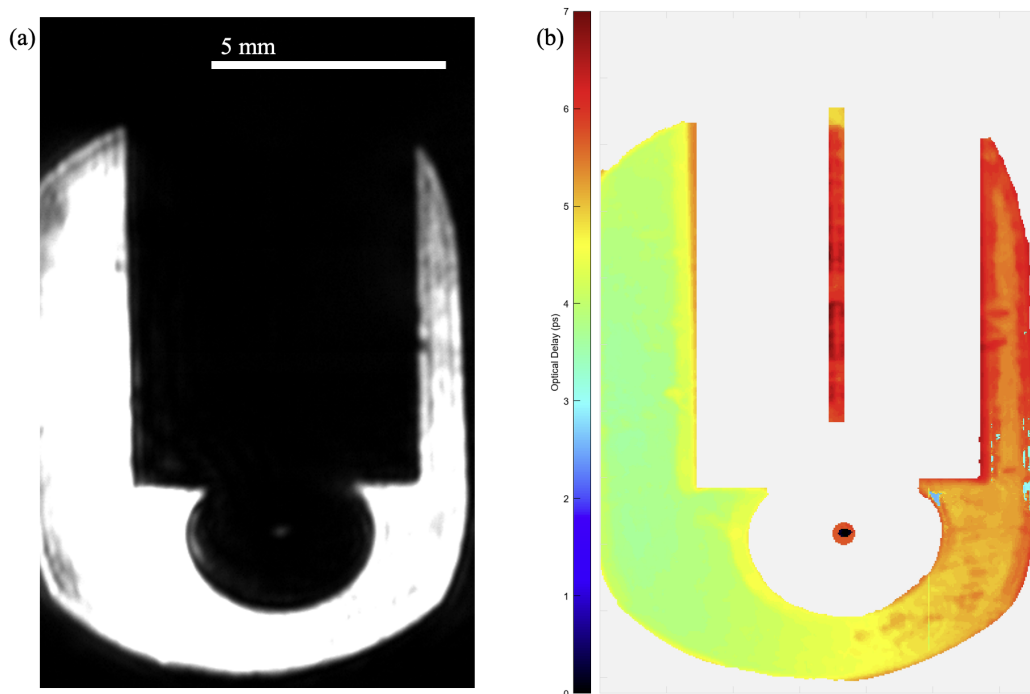


**Figure 8.** (a) Traditional Shadowgraph Image of the single bubble scene. (b) Temporally Tagged Shadowgraph (TTS) of the same scene showing the time delay of peak pixel intensity relative to the Ballistic signal.

The computed time delays are compared to visual inspection of standard shadowgraph images to measure bubble size and assess the applicability of the TTS measurements. With a known spatial resolution of  $27.3 \mu\text{m}/\text{pixel}$ , the major and minor axis are measured. As the bubble is nonspherical and bound to a flat surface, the minor axis is measured twice: first, from the lowest point to the glass rod, and second, double the distance of the lowest point to the illuminated center.

**Table 1.** Measurements of Bubble size from Shadowgraph.

	Length (mm)	Notes
Major Axis	4.06	-
Minor Axis 1	2.56	Lowest point to rod
Minor Axis 2	3.52	Double measured radius

Due to the spatiotemporal variations caused by the switch pulse angle, delays are only compared within the same column. Fig. 8(b) shows that directly beneath the bubble, the computed time delay between 4 and 5 ps. Closely examining the column leads to a mean time delay of 4.467 ps.

Applying the conversion factor of 1.097 ps/mm, using only weak-field refractive index at 800 nm at 25°C, calculates a diameter of 4.074 mm. This is in good agreement with major axis measurement. Such is expected if the bubble is axisymmetric about the vertical axis.

The signal from the glass rod center is also assessed to evaluate the TTS further. With the geometry of the borosilicate glass rod, a time delay is expected between 1.64 ps and 2.96 ps, depending on whether the center is filled with air or water, respectively. When measured, the mean time delay between the glass rod signal and the water below is 1.713 ps, slightly longer than the expected 1.64 ps for pure air in the center. Fig. 6(g-i) shows this signal to be disconnected and non-uniform, suggesting residual water deposits, which may account for this difference between the observed delay and expected dry value.

### 3.2. Frozen Bubble Plume

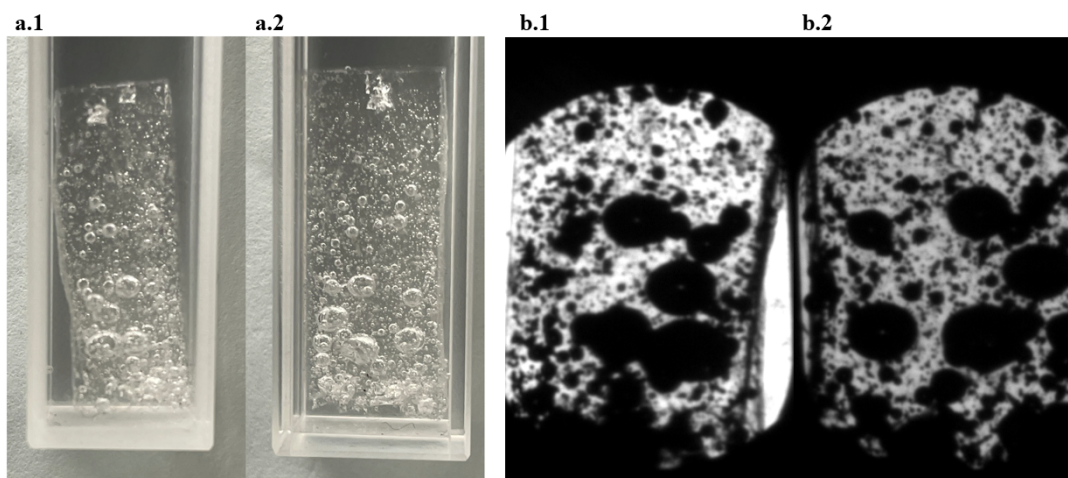


**Figure 9.** (a) Orthogonal views of a frozen bubble plume within an index-matched polymer, submerged within a 10 mm cuvette. (b) Static images when illuminated in transmission by Continuous LED.

After fully curing, the polymer was submerged and imaged under continuous white light, Fig. 9. Within the plume itself, bubbles show significant variation in size, with the largest being no greater than 3 mm. There is also notable occlusion, primarily by clusters of microbubbles blocking the centers of larger bubbles. White light imaging does reveal some optical centers, which significantly aids in locating ballistic signals. Again, with this being static and repeatable, time-gated images are taken with the polymer plume at four orientations; Fig. 10 presents select frames for one such view. Images are acquired at 1 kHz, while the delay stage moves at a speed of 0.68 ps/s, hence an observed frame rate of approximately 1.46 PHz.

Fig. 10(a-d) shows the appearance of the outline of the polymer before the ballistic signals from the centers of the frozen bubbles. With the maximum bubble diameter of 3 mm, the maximum

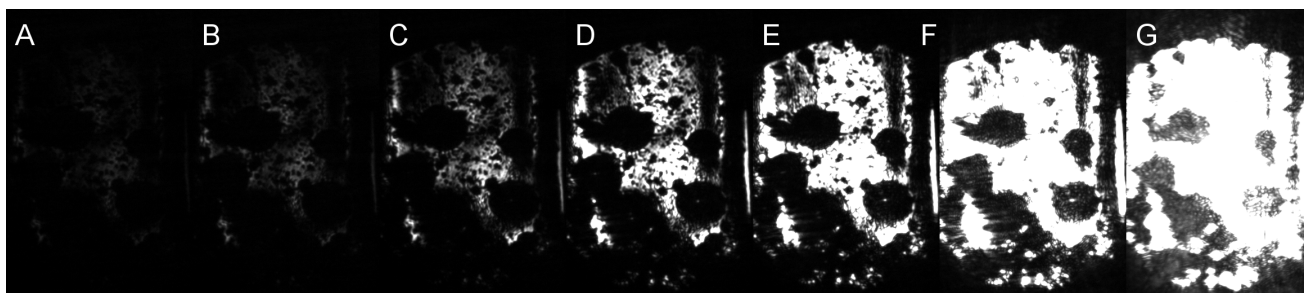


**Figure 10.** A montage of OKE time-gated images of one polymer plume view, taken in 0.55 ps intervals.

expected delay, 3.29 ps, is almost equal to the measured exposure. Combined with the diminished intensity of the ballistic signal, this phenomenon is expected. Peak intensity is, therefore, the most important quantity in evaluating temporal location. Some ballistic signals start appearing in Fig. 10d, however they become much more visible and defined in Fig. 10e. Between Fig. 10e and f, ballistic signals continue to appear, although their appearance is overshadowed by the onset of scattered snake photons, visible in the loss of definition of the edge of bubbles. Microbubbles within polymer become completely occluded by this intense scattering before the appearance of their ballistic signals. Again, this results from exposure being too long relative to the time scales concerning the smallest bubbles, even with the time finer gating resolution. Similar results were seen in Chaussonnet et al. (2021), where ballistic signals become wholly enveloped by the most intense undisturbed signals once the mean bubble cloud diameter is less than 100  $\mu\text{m}$ . Equally, the definition of ballistic signals is reduced further with greater polydispersity within a cloud. Significant poly dispersion is notable within the polymer plume (Fig. 9); hence, the loss of these signals is expected. Further loss of definition may result from striations within the polymer created during curing and post-curing processing. By Fig. 10g, approximately 3.3 ps after the first photons appear, snake photons combined with the latent undisturbed signal completely overshadow most features within the plume, similar to scattering phenomena within a whitecap.

As with the single bubble, TTS images have been produced for two orthogonal views. Once the full ROI is accounted for, the TTS is refined to focus on the discernable, unoccluded ballistic signals (Fig. 11). Due to the polymer significant polydispersity and void fraction, it is difficult to determine where a signal is undisturbed. Mean temporal measurements are therefore necessary, with carefully identified reference points. The TTS for both the displayed views shows the limited locations of the undisturbed signals. Surrounding the bubbles, a visible gradient in time delay appears within the boundaries visible in Fig. 9b. This agrees with Chaussonnet et al. (2021), where lower scattering modes from the edges of the bubble appear at a similar time to the undisturbed signals, contributing to the loss of definition.

Those with discernible centers have again been measured visually, first by edge detection followed by measurement based on a known resolution. Mean time delays of identified ballistic signals relative to the surrounding water signal are also computed and converted to diameters. It should

be noted that some of those identified are partially occluded, but as ballistic signals are conserved these have still been measured. The comparison of these measurements is in Fig. 12.

Overall, measurements by delay tend to be slightly greater than those found through edge detection. This visual inspection is prone to errors due to loss of definition at the edges, and this is only made worse with the substantial occlusion; hence, this underestimation is expected. There is a notable difference with bubble iii, with the time delay estimate being over double the estimate from edge detection. Inspection of the white-light images shows this bubble as being partially occluded with several smaller bubbles in close orbit. The assumed ballistic signal may have passed through several bubbles, increasing the observed time delay and weakening the signal. Equally, this inconsistent mean time delay may have been influenced by surrounding noise or by holographic fringes created by the polymer. This highlights the need to improve the robustness of the processing methods and preparation of the TTS. Excluding bubble iii, there is some agreement with the mean difference between the two methods at 0.105 mm with a standard deviation of 0.292 mm. It should be noted that this is for a limited number of bubbles due to highlighted difficulties in locating ballistic and undisturbed signals. Taking a greater number of similar measurements is also necessary to fully assess the viability of this technique.

#### 4. Conclusion

For the first time, Ultrafast Imaging using Optical Kerr Effect time gating has been demonstrated with bubbly scenes. Initial single bubble tests show excellent agreement with the previous computational work of Chaussonnet & Bardet (2020), experimentally capturing scattering responses similar to those calculated. Furthermore, the capability to measure bubble sizes has been tested, with results coinciding with traditional techniques, but with the ability to cover higher void fraction. Even without measurement of the ballistic signal, using an ultrashort exposure with fine temporal controls successfully removes the influence of higher-order scattering modes, preserving the definition of bubbles and submerged objects. With increased definition, existing size determination methods can still be applied with reduced uncertainty.

With a high-void fraction plume, high-order scattering modes can still be removed, and there is still agreement with Chaussonnet et al. (2021); however, there is some residual uncertainty when it comes to size determination. The 2.9 ps exposure creates a limiting factor as to size determination, as ballistic photons become overwhelmed by intense undisturbed photons. Shortening this exposure is, therefore, a priority, allowing greater confidence in measurements of smaller bubbles. Doing so would also be necessary to measure sub-Hinze scale bubbles successfully. Attempts were also made to measure occluded bubbles. While distortions increased, the majority of measurements corresponded to visual measurements. Given the degree of occlusion, the uncertainty of these visual measurements should also be questioned when evaluating the two methods.

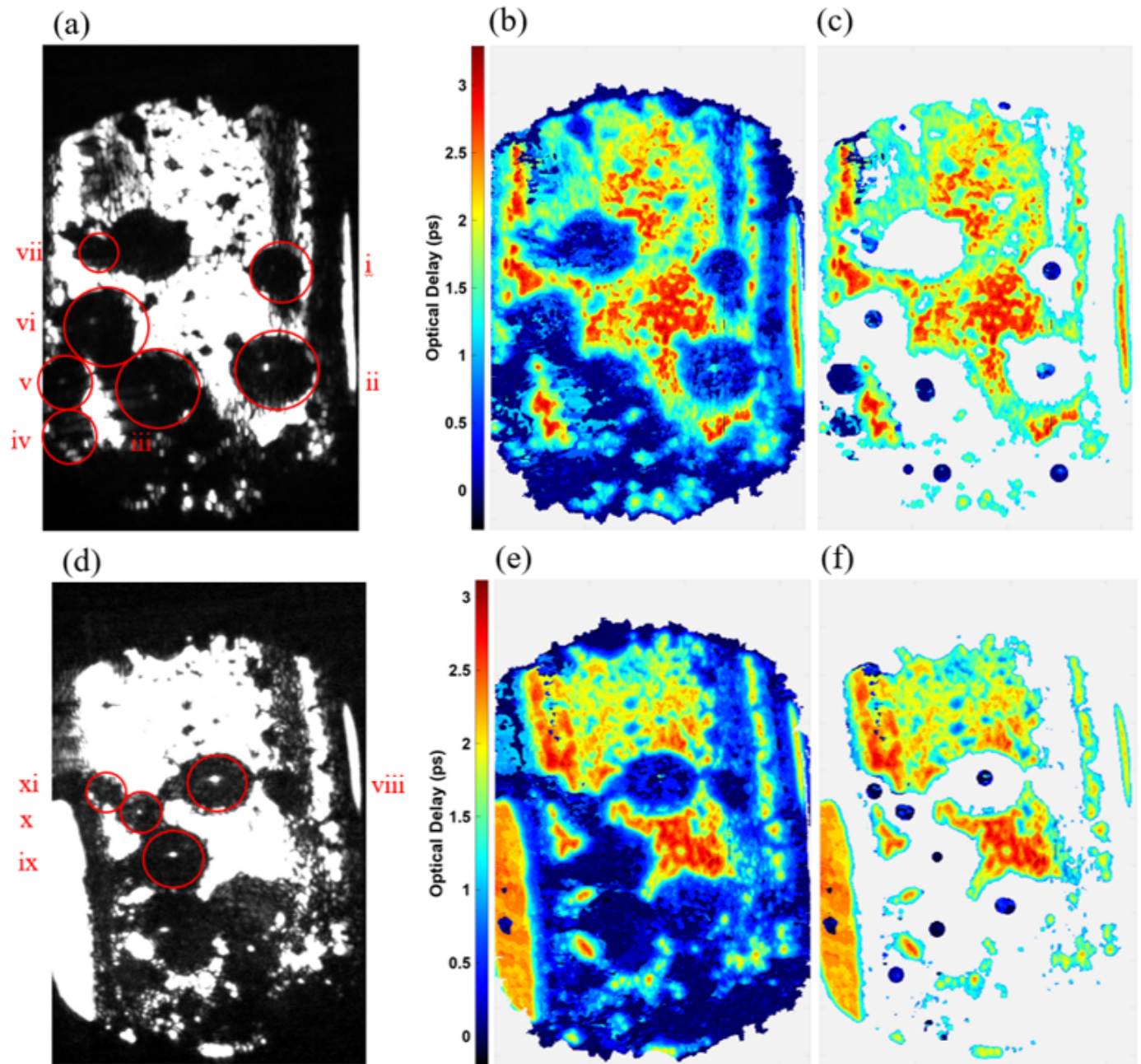


**Figure 11.** (a,d) LED illuminated images of two orthogonal views of the frozen polymer. (b) TTS image of view in (a). (c) Masked TTS (b) focuses only on ballistic signals. (e) TTS image of view in (d). (f) Masked TTS (e) focuses only on ballistic signals.

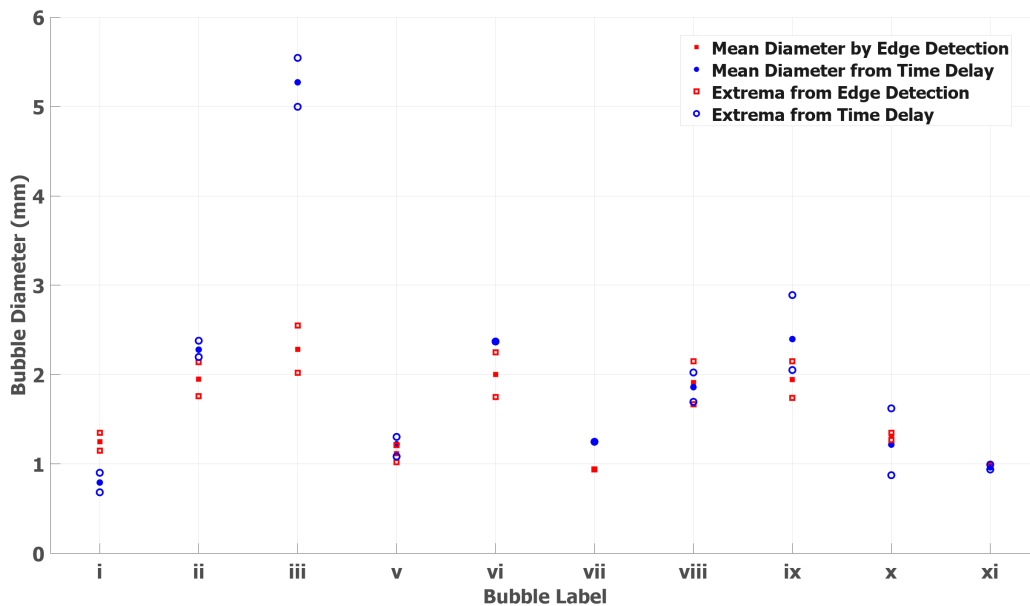


Figure 12. Comparison of size determination by edge detection, and through mean time delay. Labels and numbering correspond to those in Fig. 11a,d.

## Acknowledgements

This work was supported by ONR grant N00014-20-1-2758 managed by Dr. Woei-Min Lin. The fs system was acquired with DOD DURIP grant. Additionally, Dr. Roberto Capanna and Mr. Jack Brown, for producing the frozen polymer plumes used heavily in this work.

## Nomenclature

$\chi^{(3)}$	Third-Order Non-linear Optical Susceptibility [ $\text{m}^2/\text{V}^2$ ]
$\omega$	Incident Angular frequency [rad/s]
$\tau_o$	Orientalional Switching Time [s]
$c$	Speed of Light [m/s]
$\tilde{E}$	Electric Field Strength [V/m]
$E_0$	Peak Electric Field Strength [V/m]
$K$	Reorientational Constant
$n$	Refractive Index
$n_0$	Weak-Field Refractive Index
$cn_2^o$	First Order Corrected Orientalional Kerr Coefficient
$\Delta n$	Induced Birefringence
$\Delta n^o$	Induced Birefringence from Reorientation

$T_w$	Pulse Width [s]
$t$	Time from Excitation [s]
$z$	Path Length [m]

## References

- Aliseda, A., & Heindel, T. J. (2021). X-ray flow visualization in multiphase flows. *Annual Review of Fluid Mechanics*, 53(1), 543–567. doi: 10.1146/annurev-fluid-010719-060201
- Al-Lashi, R. S., Gunn, S. R., & Czerski, H. (2016, August). Automated processing of oceanic bubble images for measuring bubble size distributions underneath breaking waves. *Journal of Atmospheric and Oceanic Technology*, 33(8), 1701–1714. doi: 10.1175/JTECH-D-15-0222.1
- Belden, J., Ravela, S., Truscott, T. T., & Techet, A. H. (2012). Three-dimensional bubble field resolution using synthetic aperture imaging: application to a plunging jet. *Experiments in Fluids*, 53(3), 839–861. doi: 10.1007/s00348-012-1322-4
- Boyd, R. W. (2008). The intensity-dependent refractive index. In *Nonlinear optics* (p. 207–252). Elsevier. doi: 10.1016/B978-0-12-369470-6.00004-6
- Bröder, D., & Sommerfeld, M. (2007). Planar shadow image velocimetry for the analysis of the hydrodynamics in bubbly flows. *Measurement Science and Technology*, 18(8), 2513–2528. doi: 10.1088/0957-0233/18/8/028
- Brücker, C. (2000). *Piv in two-phase flow*. Von Karman Institute for Fluid Dynamics, Rhode-St-Genese, Belgium,.
- Calba, C., Méès, L., Rozé, C., & Girasole, T. (2008, July). Ultrashort pulse propagation through a strongly scattering medium: simulation and experiments. *Journal of the Optical Society of America A*, 25(7), 1541. doi: 10.1364/JOSAA.25.001541
- Chase, L. L., & Van Stryland, E. W. (1995). Section 8. 1 nonlinear refractive index. In *Optical materials*. Boca Raton, FL: CRC Press.
- Chaussonnet, G., & Bardet, P. M. (2020). Scattering of an ultrashort laser pulse by a spherical air bubble. *Optics Express*, 28(19), 27358–27358. doi: 10.1364/oe.401010
- Chaussonnet, G., Mees, L., Šormaz, M., Jenny, P., & Bardet, P. M. (2021). Modeling multiple scattering transient of an ultrashort laser pulse by spherical particles. *Journal of Computational Physics*, 457, 110696. doi: 10.1016/j.jcp.2021.110696

- Chen, L., Xu, C., Li, J., & Zhang, B. (2023, January). A 3d measurement method of bubbles based on edge gradient segmentation of light field images. *Chemical Engineering Journal*, 452, 139590. doi: 10.1016/j.cej.2022.139590
- Deane, G. B., & Stokes, M. D. (2002). Scale dependence of bubble creation mechanisms in breaking waves. *Nature*, 418(6900), 839–844. doi: 10.1038/nature00967
- Deike, L. (2022). Mass transfer at the ocean–atmosphere interface: The role of wave breaking, droplets, and bubbles. *Annual Review of Fluid Mechanics*, 54(1), 191–224. doi: 10.1146/annurev-fluid-030121-014132
- Eisenthal, K. B. (1977). Picosecond relaxation processes in chemistry. In S. L. Shapiro (Ed.), *Ultrashort light pulses* (Vol. 18, p. 275–315). Berlin, Heidelberg: Springer Berlin Heidelberg. doi: 10.1007/978-3-662-22574-5\_6
- Hessenkemper, H., & Ziegenhein, T. (2018). Particle shadow velocimetry (psv) in bubbly flows. *International Journal of Multiphase Flow*, 106, 268–279. doi: 10.1016/j.ijmultiphaseflow.2018.04.015
- Idlahcen, S., Méès, L., Rozé, C., Girasole, T., & Blaisot, J. (2009). Time gate, optical layout, and wavelength effects on ballistic imaging. *Journal of the Optical Society of America*, 26(9), 1995–1995. doi: 10.1364/josaa.26.001995
- Linne, M. A., Paciaroni, M., Gord, J. R., & Meyer, T. R. (2005). Ballistic imaging of the liquid core for a steady jet in crossflow. *Applied Optics*, 44(31), 6627. doi: 10.1364/AO.44.006627
- Liu, Y., Wang, C., Qian, Y., Sun, X., & Liu, Y. (2020). Uncertainty analysis of piv measurements in bubbly flows considering sampling and bubble effects with ray optics modeling. *Nuclear Engineering and Design*, 364, 110677. doi: 10.1016/j.nucengdes.2020.110677
- Masuk, A. U. M., Salibindla, A., & Ni, R. (2019). A robust virtual-camera 3d shape reconstruction of deforming bubbles/droplets with additional physical constraints. *International Journal of Multiphase Flow*, 120, 103088. doi: 10.1016/j.ijmultiphaseflow.2019.103088
- Mourou, G., & Malley, M. (1975). Molecular orientational relaxation times in liquids. *Optics Communications*, 13(4), 412–417. doi: 10.1016/0030-4018(75)90135-2
- Sala, K., & Richardson, M. C. (1975). Optical kerr effect induced by ultrashort laser pulses. *Physical Review A*, 12(3), 1036–1047. doi: 10.1103/PhysRevA.12.1036
- Sedarsky, D. L., Paciaroni, M. E., Linne, M. A., Gord, J. R., & Meyer, T. R. (2006, April). Velocity imaging for the liquid-gas interface in the near field of an atomizing spray: proof of concept. *Optics Letters*, 31(7), 906. doi: 10.1364/OL.31.000906

Shapiro, S. L., & Broida, H. P. (1967). Light scattering from fluctuations in orientations of  $C_2$  in liquids. *Physical Review*, 154(1), 129–138. doi: 10.1103/PhysRev.154.129